HHS Public Access

Author manuscript

Mol Pharm. Author manuscript; available in PMC 2018 October 02.

Published in final edited form as:

Mol Pharm. 2017 October 02; 14(10): 3239–3247. doi:10.1021/acs.molpharmaceut.7b00216.

ImmunoPET imaging of CD146 in murine models of intrapulmonary metastasis of non–small cell lung cancer

Christopher G. England[†,#], **Dawei Jiang**[‡,||,#], **Reinier Hernandez**[†], **Haiyan Sun**[||], **Hector F. Valdovinos**[†], **Emily B. Ehlerding**[†], **Jonathan W. Engle**[†], **Yunan Yang**[||], **Peng Huang**[‡,*], and **Weibo Cai**[†,||,§,*]

[†]Department of Medical Physics, University of Wisconsin - Madison, WI 53705, USA

[‡]Guangdong Key Laboratory for Biomedical Measurements and Ultrasound Imaging, School of Biomedical Engineering, Shenzhen University, Shenzhen 518060, China

[||]Department of Radiology, University of Wisconsin - Madison, WI 53705, USA

[§]University of Wisconsin Carbone Cancer Center, Madison, WI 53705, USA

Abstract

CD146 has been identified as an excellent biomarker for lung cancer as its overexpression in solid tumors has been linked to disease progression, invasion, and metastasis. Previously, our group described a positive correlation between ^{64}Cu-labeled YY146 uptake and increased expression of CD146 in six human lung cancer cell lines using subcutaneous tumor models. In this study, we investigate a monoclonal antibody called YY146 for immunoPET imaging of CD146 in two intrapulmonary metastasis models of non-small cell lung cancer (NSCLC). The binding and immunoreactivity of the tracer were assessed by *in vitro* assays. Radiolabeling of YY146 with the positron emitting Cu-64 (^{64}Cu-NOTA-YY146) enabled PET imaging of intrapulmonary metastasis. Mice were intravenously injected with two-million tumor cells, and CT imaging was used to verify the presence of lung metastases. ^{64}Cu-NOTA-YY146 was injected into tumor-bearing mice and animals were subjected to PET/CT imaging at 4, 24, and 48 h post-injection. Both the average and maximum lung PET signal intensities were quantified and compared between high and low CD146-expressing metastases. Further validation was accomplished through immunofluorescence imaging of resected tissues with CD31 and CD146. In flow cytometry, YY146 revealed strong binding to CD146 in H460 cells due to its high expression, with minimal binding to CD146-low expressing H358 cells. Both YY146 and NOTA-YY146 showed similar binding, suggesting that NOTA conjugation did not elicit any negative effects on its

[*]Corresponding Author: Weibo Cai, Ph.D., Address: Departments of Radiology and Medical Physics, University of Wisconsin - Madison, Room 7137, 1111 Highland Ave, Madison, WI 53705-2275, USA. wcai@uwhealth.org; Phone: 608-262-1749; Fax: 608-265-0614. Peng Huang, Ph.D., Address: Nanhai Ave 3688, Guangdong Key Laboratory for Biomedical Measurements and Ultrasound Imaging, School of Biomedical Engineering, Shenzhen University, Shenzhen, Guangzhou, 518060, P.R. China. peng.huang@szu.edu.cn; Phone: 86-0755-86671911.

[#]These authors contributed equally to this work.

Disclosure Statement

The authors declare that they have no conflicts of interest.

Supporting Information

The authors have included tables with the PET ROI values and control animal figure. The Supporting Information is available free of charge on the ACS Publication website.

binding affinity. Imaging of ^{64}Cu-NOTA-YY146 in H460 tumor-bearing mice revealed rapid, persistent, and highly-specific tracer accumulation. Uptake of ^{64}Cu-NOTA-YY146 in the whole lung was calculated for H460 and H358 as 7.43 ± 0.38 and 3.95 ± 0.47 %ID/g at 48 h post-injection (n=4, $p<0.05$), while the maximum lung signal was determined to be 13.85 ± 1.07 (H460) and 6.08 ± 0.73 %ID/g (H358) at equivalent time points (n=4, $p<0.05$), respectively. To ensure the specificity of the tracer, a non-specific antibody was injected into H460 tumor-bearing mice. *Ex vivo* biodistribution and immunofluorescence imaging validated the PET findings. In summary, ^{64}Cu-NOTA-YY146 allowed for successful imaging of CD146-expressing intrapulmonary metastases of NSCLC in mice. This preliminary study provides evidence supporting the future clinical utilization of ^{64}Cu-NOTA-YY146 for possible treatment monitoring of CD146-targeted therapy or improving patient stratification.

Graphical Abstract

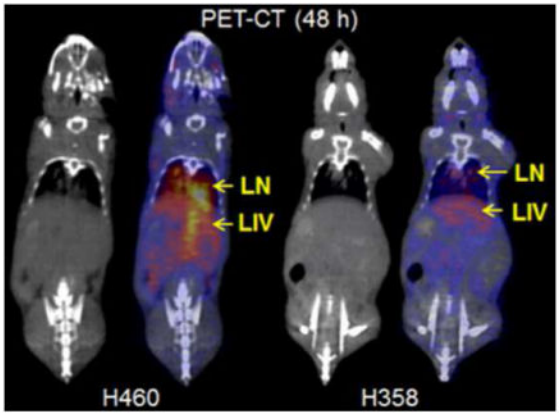

Keywords

Positron emission tomography (PET); non-small cell lung cancer; intrapulmonary metastasis; copper-64 (^{64}Cu); YY146; CD146; immunoPET

INTR ODUCTION

While treatments and preventative strategies are continually improving, lung cancer remains the leading source of cancer-related deaths in both male and females.[1] According to the American Cancer Society, cases of lung cancer in the U.S. are expected to surpass 225,000, along with more than 155,000 associated deaths in 2017. In addition to being a highly lethal disease, lung malignancies are the most common type of cancer worldwide contributing ~13% of new cancer cases diagnosed each year. The incidence and death rates have steadily declined over the last decade, yet 5-year survival rates remain unfavorably low due to several reasons, including ineffective screening techniques, the aggressive nature of lung malignancies, and the rapid development of chemoresistance.[2] The relative 5-year survival rates are dependent on disease stage, with an average of 18% across all stages and individual values of 55%, 28%, and 4% for localized, regional, and distant (metastatic) disease,

respectively. For these reasons, there is an urgent need for new or improved clinical strategies for early detection and treatment of lung cancer.

Non-small cell lung cancer (NSCLC) remains difficult to diagnose, as symptoms often do not appear until advanced tumor stages are reached, and traditional screening methods often require multiple tests to determine tumor localization, staging, and aggressiveness.[3] Molecular imaging strategies, like positron emission tomography (PET), have already shown immense clinical utility for the diagnosis of lung cancer; however, there is still a need for marker-specific tracers in this disease. Currently, combined computed tomography (CT) and PET with ^{18}F-FDG (FDG-PET) are employed for diagnosing most cases of lung cancer,[4] yet the low specificities of CT (average, 73%)[5] and FDG-PET (average, 79%; range, 52–100%)[6] can limit the detection of patient malignancies, especially individuals with smaller malignancies of <1.5 cm in diameter. Intrapulmonary metastases, also known as multifocal or satellite nodules, occurs when cells from the primary lung tumor spread to other regions of the lungs.[7] Intrapulmonary metastases are difficult to differentiate on a molecular scale from the primary tumor, yet there is hope that newer imaging agents may allow physicians to better visualize these metastatic lesions. Recently, the advent of new PET tracers has shown potential benefits through targeting of cellular proliferation with ^{18}F-fluorothymidine (^{18}F-FLT) and tumor hypoxia using ^{18}F-fluoromisonidazole (^{18}F-FMISO);[8, 9] however, these tracers have also shown some limitations and require further optimizations.

CD146 (cluster of differentiation 146), also known as MUC18 or MCAM, has been associated with increased tumor aggressiveness in a number of malignancies arising from lung,[10] liver,[11] gastric,[12] breast,[13] colon,[14] and brain tissues.[15] In healthy tissues, CD146 is an important mediator of cell-cell interactions and is normally expressed at low levels on the surface of most endothelial cells found in humans, along with some smooth muscle and follicular dendritic cells.[16, 17] For most cancers, elevated CD146 expression is associated with increased metastatic potential and decreased survival rates. In a recent investigation on the connection between CD146 and overall survival in patients with lung adenocarcinomas, Oka *et al.* found that males were more likely to have CD146-high tumors and that CD146 expression decreased the 5-year survival rates by ~35% (84.4 to 50.0% for CD146^{-} and CD146^{+} patients, respectively).[18] Thus far, CD146 expression has been detected in 50–75% of lung cancers,[10] suggesting that it may hold immense potential to serve as a diagnostic and prognostic biomarker in lung cancer.

Previously, we employed a rapid immunization approach to generate an antibody targeting CD146 called YY146.[19] PET tracers have recently been developed for the imaging of CD146 in brain and hepatocellular cancers,[15, 20] demonstrating differential uptake in CD146-expressing malignancies. Next, we described a positive correlation between ^{64}Cu-labeled YY146 uptake and increased CD146 expression in six human lung cancer cell lines (including the two cells explored in this study) using subcutaneous tumor models.[21] While PET imaging of the lungs is inherently difficult due to the anatomical location, we hypothesized that CD146 would be an excellent biomarker for targeting in lung cancer using an intrapulmonary metastasis model. Therefore, we developed and characterized the potential of our CD146 PET tracer, based on our novel CD146 antibody (YY146), to image intrapulmonary metastases of NSCLC. We demonstrate successful visualization of CD146-

expressing lung nodules *in vivo* using noninvasive immunoPET imaging. Hence, we believe this tracer has the potential to be a valuable diagnostic tool in lung cancer, providing invaluable molecular information to diagnose or guide treatment-related decisions.

EXPERIMENTAL SECTION

Cell culture

Two human lung cancer cell lines, H460 and H358, were obtained from the American Type Culture Collection (ATCC, Manassas, VA, USA). Cell lines were cultured according to the manufacturer's suggestion using Roswell Park Memorial Institute (RPMI)-1640 medium supplemented with 10% non-heat-inactivated FBS (Gibco, Thermo Fisher Scientific, Waltham, MA, USA) and 1% penicillin-streptomycin solution (Gibco, Thermo Fisher Scientific, Waltham, MA, USA) in a humidified incubator at 37 °C with 5% CO_2.

Radiolabeling of YY146

Radiolabeling of YY146 with ^{64}Cu was accomplished through conjugation of the chelator p-SCN-Bn-NOTA (NOTA; Macrocyclics, Dallas, TX, USA) to the antibody. This procedure was previously described.[21, 22] Briefly, 2–4 mg of YY146 (in PBS) was adjusted to pH ~8.5 using 0.1M Na_2CO_3. NOTA was dissolved in DMSO and added to the antibody solution at a molar ratio of 1:10 (YY146:NOTA) and allowed to react for 2–3 h at room temperature. PD-10 columns (GE Healthcare, Aurora, OH, USA) were used to purify NOTA-YY146 from unconjugated NOTA. ^{64}Cu was produced in a CTI RDS 112 cyclotron via $^{64}Ni(p,n)^{64}Cu$ reaction and isolated via cation exchange chromatography in 0.1 M HCl. For radiolabeling, 150–200-μg of NOTA-YY146 was mixed with 74–148 MBq (2–4 mCi) of $^{64}CuCl_2$ in 300-μL of 0.1 M sodium acetate buffer (pH 4.5) at for 30 min at 37 °C. ^{64}Cu-NOTA-YY146 were purified using PD-10, and the fractions were collected and filtered through a 0.2-μm filter before injection into mice. The specific activity is approximately 2 Ci per μmol and ~15 μg antibody was injected into each mouse. Radiolabeled IgG (ThermoFisher Scientific, Waltham, MA, USA) was performed using the same procedures above.

Flow cytometry

The binding and immunoreactivity of the antibody to CD146 was assessed by flow cytometry in H460 and H358 cells. First, cells were harvested at ~70% confluency, counted, and resuspended in ice-cold PBS at 1×10^6 cells per mL. Cells were incubated for 30 min on ice with either PBS, 5 μg/mL YY146, 25 μg/mL YY146, 5 μg/mL NOTA-YY146, or 25 μg/mL NOTA-YY146. After washing and centrifugation, cells were incubated with 5 μg/mL of Cy3-labeled goat anti-mouse secondary antibody for 30 min on ice. Lastly, cells were washed and the binding efficiencies were analyzed using the MACSQuant cytometer (Miltenyi Biotech, Germany) and the data were analyzed using FlowJo (Tree Star, Inc., Ashland, OR, USA).

Saturation binding assay

The equilibrium dissociation constant (K_D) and receptor density were calculated from a receptor saturation binding assay. In the assay, H460 and H358 cells were seeded in a 96-

well plate at 1×10^5 cells per well and increasing concentrations of ^{64}Cu-NOTA-YY146 in PBS were added to each well (range 0.03 – 100 nM). Cells were incubated with the radiolabeled antibody for 2 h at room temperature. For determination of nonspecific binding, 1 μmol of unlabeled YY146 was added to corresponding wells. After a 2 h incubation, wells were washed three times with PBS, and the cells were harvested and counted using an automated γ-counter (PerkinElmer, Waltham, MA, USA). The total binding and nonspecific binding isotherms were plotted using the GraphPad Prism software 7.00 (La Jolla, CA, USA), which provided the B_{max} and K_D values that allowed for calculation of receptor density.

Development of animal model

All animal studies were conducted under the approval of the University of Wisconsin Institutional Animal Care and Use Committee. For implantation, cells were grown to 70% confluency and detached using Accutase (Thermo Fisher, Waltham, MA, USA). After washing and centrifugation, cells were resuspended in 1 mL of PBS at a concentration of 5×10^6 cells/mL. Next, four-to-five week old female athymic mice (Envigo, Cambridgeshire, United Kingdom) were intravenously injected with 200 μL of H460 or H358 cancer cells. From previous studies, we determined that lung nodules developed between 3–6 weeks post-implantation; thus, CT imaging was used verify the presence and monitor the development of lung nodules starting at day 21. For this study, mice were used between 27–35 days after injection of cancer cells upon confirmation of lung nodules by CT.

PET/CT imaging and image analysis

H460 and H358 tumor-bearing mice were intravenously injected with 7.4–11.1 MBq of ^{64}Cu-NOTA-YY146. PET images were acquired at 4, 24, and 48 h post-injection of ^{64}Cu-NOTA-YY146 or ^{64}Cu-NOTA-IgG using an Inveon microPET/CT (Siemens Medical Solutions, Knoxville, TN, USA). Mice were placed in prone position in the scanner after anesthesia was induced and maintained with 1–2% isoflurane. PET scans of 20–40 million coincidence events were acquired per mouse for every static PET emission scan with an energy window of 350–650 keV, a time window of 3.43 ns, and resolution of ~1.5 mm. For PET/CT imaging, CT images were obtained using the following settings for anatomical registration and attenuation correction: 80 kV, 900 μA, and a nominal resolution of 105 μm. PET images were reconstructed using the 3D ordered subset expectation maximization (OSEM3D) algorithm and quantitative region of interest analyses were performed in the Inveon Acquisition Workplace (Siemens Medical Solutions, Malvern, PA, USA). Data were reported as the percentage of injected dose per gram (%ID/g).

Ex vivo biodistribution studies

Ex vivo biodistribution studies were performed after the final imaging time point at 48 h after injection. First, mice were euthanized by CO_2 asphyxiation and cervical dislocation. The portions of the lung that contained nodules, blood, and major organs and tissues were collected and weighed before the activities were counted in an automatic γ-counter, and the recorded as %ID/g (mean ± SD).

Immunofluorescence staining

After euthanizing the mice, the lung was visually inspected for the presence of tumor nodules. were surgically extracted and preserved for immunofluorescence staining using procedures previously described.[21] Briefly, tissues were embedded in Tissue-Tek optimal cutting temperature (O.C.T.) compound (Sakura Finetek, Torrance, CA, USA) for histological sectioning at the Experimental Pathology Laboratory (University of Wisconsin Carbone Center, Madison, WI, USA). Tissue slides of 5 μm thickness were fixed in ice-cold acetone for 15 min and dried at room temperature for 15 min. Next, slides were washed in PBS and blocked in 2.5% donkey serum for 1 h at room temperature. After blocking, slides were incubated for 12 h at 4 °C with the CD31 (Novus Biologicals, Littleton, CO, USA) and CD146 (YY146) primary antibodies at concentrations of 2 μg/mL and 10 μg/mL, respectively. Next, slides were washed 3-times with PBS-T (PBS with 0.1% Tween 20) for 10 min before addition of secondary antibodies. The slides were next incubated with Cy3-labeled donkey anti-rat and AlexaFluor488-labeled goat anti-mouse at room temperature for 2 h, then washed 3-times with PBS-T and 3-times with PBS before coverslipped using Vectashield mounting medium for fluorescence microscopy with 4′,6-diamidino-2-phenylindole (DAPI; Vector Laboratories, Burlingame, CA, USA). Imaging was performed on the Nikon A1R confocal microscope (Nikon Instruments, Melville, NY, USA).

Statistical Analysis

Quantitative data were expressed as the mean ± standard deviation (SD). A 95% confidence interval was used with $p<0.05$ being considered statistically significant.

RESULTS

Development of ^{64}Cu-NOTA-YY146

Development and *in vitro* characterization of the PET tracer ^{64}Cu-NOTA-YY146 were performed prior to injection into tumor-bearing mice. To successfully radiolabel YY146, a bifunctional chelator (NOTA) was conjugated to the antibody through the exposed lysine residues. After purification with PD-10 columns, the radiolabeling yield of ^{64}Cu-NOTA-YY146 was calculated to be ≥ 85%, with a radiochemical purity of over 95%. ^{64}Cu-NOTA-YY146 was then utilized to image lung cancer metastases using two lung cancer cell lines, known to express high (H460) or low (H358) levels of CD146. In addition, a nonspecific tracer (^{64}Cu-NOTA-IgG) was obtained with the same method and similar radiolabeling efficiency.

In Vitro Characterization of ^{64}Cu-NOTA-YY146

In a previous study, we showed that H460 and H358 expressed significantly different levels of CD146 *in vitro* by Western blot analysis. [21] H460 cells were shown to highly express surface CD146, while H358 was found to express CD146 at levels much lower than that of H460. Flow cytometry was performed to validate the cell binding and immunoreactivity of YY146 towards CD146 expressed on H460 and H358 cells. Additionally, this assay determined the impact that conjugation of the chelator NOTA would have on YY146's binding affinity. In H460 cells, YY146 showed excellent cell binding at both 5 μg/mL and

25 μg/mL in a concentration-dependent manner. This appeared as a stronger shift to the right in the fluorescent histograms with the higher concentration of antibody at 25 μg/mL (Figure 1), as indicated by the positive shift in Cy3 signal. Conjugation of the chelator did not affect the interaction between the antibody and CD146, as there were minimal changes in signal between YY146 and NOTA-YY146 at both concentrations in H460 cells. For H358 cells, known to express lower levels of CD146, no shift in Cy3 signal compared to the control was noticeable through flow cytometry (Figure 1).

The affinity of ^{64}Cu-NOTA-YY146 for CD146 was determined via a receptor saturation binding assay (Figure 2). Antibody affinity is typically reported as the equilibrium dissociation constant (K_D), and was calculated as 2.84 ± 0.53 nM in H460 cells. This value suggests a strong binding affinity between ^{64}Cu-NOTA-YY146 and CD146. Additionally, the receptor density of CD146 on the surface of H460 cells was found to be ~9.9×10^5 receptors per cell. Due to the low expression levels of CD146 on H358 cells, no reliable K_D or receptor density values were obtained for this cell line.

PET Imaging of CD146 in Intrapulmonary Metastasis Model of NSCLC

The intrapulmonary metastasis model of NSCLC was created by intravenous injection of lung cancer cells in athymic nude mice. CT imaging was used to validate and monitor the presence of lung nodules and representative images from H460 and H358 mice are shown in Figure 3. The metastases (M), liver (LIV), and heart (H) have been marked for convenience.

Small nodules are visible in the thoracic cavity of both H460 (Figure 3A) and H358 (Figure 3B) tumor-bearing mice. Additionally, a radiolabeled non-specific IgG was injected into H460 tumor-bearing mice to ensure the specificity of the targeted tracer (Figure 3C). CT scans of a healthy mouse have been provided as a control, which showed no nodules in the lungs (Figure S1).

In H460 tumor-bearing mice, lung signal could be easily differentiated from that of the heart at the initial time points, 4 h after injection of the ^{64}Cu-NOTA-YY146. Since the intrapulmonary metastases were dispersed throughout different portions of the lung, the quantification results were reported and compared between groups as whole lung (with tumor metastases) versus the maximum lung signal, with the latter being indicative of the maximum intensity value for the brightest metastasis (Figure 4). For H460 tumor-bearing mice, ^{64}Cu-NOTA-YY146 uptakes in the whole lung were 5.63 ± 0.36, 6.15 ± 0.50, and 7.43 ± 0.38 %ID/g at 4, 24, and 48 h post-injection (n=4), respectively. In parallel, the maximum tumor signals also increased over time from 10.85 ± 0.60 %ID/g at 4 h post-injection to 13.85 ± 1.07 %ID/g at 48 h post-injection. In mice bearing H358 tumors, the average lung signal was significantly lower at each time point, with 3.50 ± 0.27, 3.98 ± 0.47, and 3.95 ± 0.47 %ID/g at 4, 24, and 48 h post-injection (n=4, $p \leq 0.01$ when compared with the H460 group), respectively. Concordantly, the maximum uptakes were also significantly lower at 5.21 ± 0.83, 5.38 ± 0.61, and 6.08 ± 0.73 %ID/g at 4, 24, and 48 h post-injection (n=4, $p \leq 0.05$), respectively. The maximum tumor values obtained for H460 were approximately two-fold higher than those found in the H358 model. Imaging in H460 tumor-bearing mice with ^{64}Cu-NOTA-IgG revealed tracer uptake in the whole lung was 12.47 ± 0.12, 8.27 ± 0.55, and 4.6 ± 0.70 %ID/g at 4, 24, and 48 h post-injection. The maximum tumor values

were 15.2 ± 0.80, 11.67 ± 0.70, and 6.57 ± 1.42 %ID/g at 4, 24, and 48 h post-injection, respectively (n=4). While initial uptake of ^{64}Cu-NOTA-IgG was high in the whole lung and intrapulmonary metastases, it was non-specific and rapidly declined. Tracer uptake was significantly higher in H460 tumor-bearing mice injected with ^{64}Cu-NOTA-YY146 (n=4) in comparison with non-specific tracer by 48 h post-injection, indicative of the high affinity and specificity of our novel CD146 imaging agent.

^{64}Cu-NOTA-YY146 uptake in other organs was determined and the time-activity curves shown in Figure 5. As expected, signal from the blood, liver, spleen, and kidneys steadily declined in both tumor models, while muscle signal remained constantly low. Blood signal was similar between the two models at 4 h post-injection with values of 11.91 ± 0.70 and 10.24 ± 0.80 for H460 and H358, respectively. After the final imaging time point at 48 h post-injection, mice were euthanized and the blood along with major organs and tissues were excised for *ex vivo* validation. Biodistribution studies showed similar findings to PET imaging results (Figure 6). A statistically significant difference in tumor signal was found between H460 and H358 models (n=4, $p \leq 0.01$), further corroborating the PET data. Blood and liver signals correlated well with the PET data, as well. Minimal uptake was found in the pancreas, stomach, intestines, brain, and muscle.

Immunohistochemistry

Immunofluorescence staining of tissue sections further correlated the PET imaging results with *in situ* CD146 expression (Figure 7). Tissue sections of the lung containing tumor nodules were co-stained for CD146 and the vasculature marker CD31. In H460 tumor-bearing mice, marked CD146 staining was found throughout the slide, which validates the *in vivo* PET and *ex vivo* biodistribution findings. As expected, H358 tissue sections showed minimal staining of CD146 that was associated with background signal. In both tumor models, CD31 and DAPI staining verified the presence of vasculature and cell nuclei, respectively.

DISCUSSION

Lung cancer accounts for nearly 13% of patients diagnosed with cancer every year, making it the most preventable forms of cancer worldwide.[1] In 2017, lung cancer will account for 26% of all cancer-related deaths in the U.S. While pancreatic malignancies are the most lethal cancers, lung cancer accounts for nearly 3-fold more deaths annually. In more than 70% of patients, lung cancer is diagnosed after the disease has become locally advanced or metastatic, a stage in which survival is significantly reduced. The advent of newer approaches for detection and treatment of lung cancer will likely decrease its lethality. For this reason, there is an urgent need for novel strategies to assist in cancer detection, treatment monitoring, and patient stratification. In the realm of cancer diagnostics, immunoPET imaging has shown remarkable growth in the last decade due to improvements in fields like antibody manufacturing and isotope production.

CD146 is a unique target as its expression has been linked to increased metastatic potential in many cancers. Additionally, it has been targeted for therapeutic purposes,[23] suggesting that CD146-targeted imaging agents may allow for monitoring of treatment response in the

future. In this study, ^{64}Cu-NOTA-YY146 allowed for a rapid and clear delineation of CD146-expressing intrapulmonary metastases. Preceding the imaging studies, the tracer was developed by radiolabeling of the murine anti-human CD146 antibody previously developed in our laboratory, known as YY146, with ^{64}Cu.[19, 24] For radiolabeling, the antibody was conjugated to the chelator through conjugation of thiocyanate-modified NOTA with free lysine residues in the antibody. Since attachment of the chelator showed no ill effects on cell binding through flow cytometry (Figure 1), it may be assumed that the lysine residues located away from the binding site of YY146.[25–27] Additionally, the tracer was highly stable *in vivo* as minimal bladder signal was visible post-injection.

Several *in vitro* assays were performed to study the expression of CD146 and the binding affinity of YY146. Saturation binding assay unveiled the high affinity of YY146 towards CD146 expressed in the H460 cell line with a K_D value of 2.84 ± 0.53 nM (Figure 2). This value was within the expected range and confirmed the strong binding affinity of the antibody; most antibodies display K_D values in the range of 10^{-6} to 10^{-9} M, with antibodies showing the highest affinity being ~10^{-12} M. [28]. Additionally, a receptor density of CD146 on H460 cells was calculated to be ~9.9×10^5 receptors per cell, which guarantees a successful implementation of imaging studies, where expression level of more than 10^5 receptors per cell is considered appropriate.[29, 30] Hence, given the strong binding affinity of ^{64}Cu-NOTA-YY146 and high receptor density of CD146 on H460 cells, ^{64}Cu-NOTA-YY146 would be expected to allow for optimal *in vivo* PET imaging of CD146 expression.

Indeed, PET imaging revealed high tracer uptake in CD146-expressing H460 tumors, while significantly lower uptake was detected in H358 tumors (Figure 3). The values were within expected ranges as we previously investigated ^{64}Cu-NOTA-YY146 in multiple subcutaneous models of lung cancer.[21] In subcutaneously-implanted H460 tumors, tracer uptake peaked at 48 h post-injection with 20.1 ± 2.86 %ID/g. The maximum tumor signal in the lung was calculated as 13.85 ± 1.07 %ID/g in H460 tumor-bearing mice (Figure 4), suggesting a 25–30% decrease in tracer accumulation from the subcutaneous model previously investigated.[19] Previous studies have shown that orthotopic tumors display significantly decreased vasculature, including functional blood and lymphatic vessels, in comparison to subcutaneous tumors.[31] Hence, this difference in overall tumor signal could be attributed to well-known variations in the vasculature and overall tumor size found between these models. Furthermore, given the small size of the lung nodules (~1 mm), partial volume effects could contribute to the significant underestimation of the tumor uptake as determined by PET. Such systematic errors are inherent to the PET quantification of small structures and could account for the significant variation in ^{64}Cu-NOTA-YY146 accretion between the tumor types.

The lung nodule model more closely resembles the situation encountered in patients than subcutaneous tumor models, as the disease may spread locally throughout the lung or move to other organs. Previous studies have shown the benefits of injecting cancer cells intravenously as methods to study highly metastatic lung malignancies.[32–34] While subcutaneous tumors display the high reproducibility required for assessing antitumor agents, orthotopic tumors models have a significantly broader range of applications as the tumors establish heterogeneous microenvironments and show high metastatic potential.[35]

For lung cancer imaging, the long circulation half-life of antibodies may pose a potential limitation due to the strong heart signal.[36] CT was utilized in this study to discern blood pool signal in the heart from the lungs. Such limitation concerning the high blood pool activity found with immunoPET may be overcome by imaging at later time points allowing for better delineation of lung signal from that of the heart. However, the relatively short half-life of ^{64}Cu ($t_{1/2}$: 12.7 h) precludes long-term imaging,[37] yet isotopes with longer half-lives like ^{89}Zr ($t_{1/2}$: 78.4 h) are becoming more accessible to researchers across the globe. Additionally, it may be possible to actively diminish the blood pool signal at the optimal time point (48 h post-injection in this study) to better visualize the lungs without CT by removing excess antibody tracer from circulation using specific intravenous immunoglobulins.[38] A third viable option may be the use of antibody Fab or Fab'$_2$ fragments of YY146 that retain great binding affinity and specificity towards CD146, but present pharmacokinetic profiles that are more amenable (a.k.a. shorter blood circulation half-life and renal excretion) for thoracic PET imaging.

CONCLUSIONS

ImmunoPET imaging has become an essential component to understanding the function and biodistribution of antibodies *in vivo*. In this study, a murine antibody targeting human CD146 radiolabeled with ^{64}Cu was successfully characterized and employed for imaging of intrapulmonary metastasis in a murine model of NSCLC. ^{64}Cu-NOTA-YY146 showed rapid, persistent, and highly specific uptake in CD146-expressing H460-derived lung metastases, while H358 metastases with low CD146 expression displayed decreased uptake of the tracer. Expression of CD146 is ubiquitous in many other cancers, suggesting that CD146-based tracers may play a potential role in clinical imaging of cancer in helping to improve early and accurate diagnosis, monitoring of therapeutic response, and potentially enhancing patient stratification.

Supplementary Material

Refer to Web version on PubMed Central for supplementary material.

Acknowledgments

This work was supported, in part, by the University of Wisconsin - Madison, the National Institutes of Health (NIBIB/NCI 1R01CA169365, 1R01EB021336, P30CA014520, 5T32GM08349, T32CA009206, T32GM008505), the National Science Foundation (DGE-1256259), the American Cancer Society (125246-RSG-13-099-01-CCE), and the National Science Foundation of China (81401465, 51573096).

References

1. Cancer Facts & Figures 2016. American Cancer Society; Atlanta, GA: 2016.
2. Heuvers ME, Hegmans JP, Stricker BH, Aerts JG. Improving lung cancer survival; time to move on. BMC Pulm Med. 2012; 12(1):77. [PubMed: 23234250]
3. Neal RD, Robbe IJ, Lewis M, Williamson I, Hanson J. The complexity and difficulty of diagnosing lung cancer: findings from a national primary-care study in Wales. Prim Health Care Res Dev. 2015; 16(5):436–49. [PubMed: 25482333]

4. Hochhegger B, Alves GR, Irion KL, Fritscher CC, Fritscher LG, Concatto NH, Marchiori E. PET/CT imaging in lung cancer: indications and findings. J Bras Pneumol. 2015; 41(3):264–74. [PubMed: 26176525]
5. Church TR, Black WC, Aberle DR, Berg CD, Clingan KL, Duan F, Fagerstrom RM, Gareen IF, Gierada DS, Jones GC, Mahon I, Marcus PM, Sicks JD, Jain A, Baum S. National Lung Screening Trial Research T. Results of initial low-dose computed tomographic screening for lung cancer. N Engl J Med. 2013; 368(21):1980–91. [PubMed: 23697514]
6. Schrevens L, Lorent N, Dooms C, Vansteenkiste J. The role of PET scan in diagnosis, staging, and management of non-small cell lung cancer. Oncologist. 2004; 9(6):633–43. [PubMed: 15561807]
7. Oliaro A, Filosso PL, Cavallo A, Giobbe R, Mossetti C, Lyberis P, Cristofori RC, Ruffini E. The significance of intrapulmonary metastasis in non-small cell lung cancer: upstaging or downstaging? A re-appraisal for the next TNM staging system. Eur J Cardiothorac Surg. 2008; 34(2):438–443. [PubMed: 18502660]
8. Szyszko TA, Yip C, Szlosarek P, Goh V, Cook GJ. The role of new PET tracers for lung cancer. Lung Cancer. 2016; 94:7–14. [PubMed: 26973200]
9. Bollineni VR, Kramer GM, Jansma EP, Liu Y, Oyen WJ. A systematic review on [(18)F]FLT-PET uptake as a measure of treatment response in cancer patients. Eur J Cancer. 2016; 55:81–97. [PubMed: 26820682]
10. Kristiansen G, Yu Y, Schluns K, Sers C, Dietel M, Petersen I. Expression of the cell adhesion molecule CD146/MCAM in non-small cell lung cancer. Anal Cell Pathol. 2003; 25(2):77–81. [PubMed: 12632016]
11. Jiang G, Zhang L, Zhu Q, Bai D, Zhang C, Wang X. CD146 promotes metastasis and predicts poor prognosis of hepatocellular carcinoma. J Exp Clin Cancer Res. 2016; 35:38. [PubMed: 26928402]
12. Liu WF, Ji SR, Sun JJ, Zhang Y, Liu ZY, Liang AB, Zeng HZ. CD146 expression correlates with epithelial-mesenchymal transition markers and a poor prognosis in gastric cancer. Int J Mol Sci. 2012; 13(5):6399–406. [PubMed: 22754372]
13. Zeng Q, Li W, Lu D, Wu Z, Duan H, Luo Y, Feng J, Yang D, Fu L, Yan X. CD146, an epithelial-mesenchymal transition inducer, is associated with triple-negative breast cancer. Proc Natl Acad Sci U S A. 2012; 109(4):1127–32. [PubMed: 22210108]
14. Liu D, Du L, Chen D, Ye Z, Duan H, Tu T, Feng J, Yang Y, Chen Q, Yan X. Reduced CD146 expression promotes tumorigenesis and cancer stemness in colorectal cancer through activating Wnt/beta-catenin signaling. Oncotarget. 2016; 7(26):40704–40718. [PubMed: 27302922]
15. Hernandez R, Sun H, England CG, Valdovinos HF, Barnhart TE, Yang Y, Cai W. ImmunoPET Imaging of CD146 Expression in Malignant Brain Tumors. Mol Pharm. 2016; 13(7):2563–70. [PubMed: 27280694]
16. Bardin N. Identification of CD146 as a component of the endothelial junction involved in the control of cell-cell cohesion. Blood. 2001; 98(13):3677–3684. [PubMed: 11739172]
17. Anfosso F, Bardin N, Vivier E, Sabatier F, Sampol J, Dignat-George F. Outside-in signaling pathway linked to CD146 engagement in human endothelial cells. J Biol Chem. 2001; 276(2): 1564–9. [PubMed: 11036077]
18. Oka S, Uramoto H, Chikaishi Y, Tanaka F. The Expression of CD146 Predicts a Poor Overall Survival in Patients with Adenocarcinoma of the Lung. Anticancer Res. 2012; 32(3):861–864. [PubMed: 22399604]
19. Yang Y, Hernandez R, Rao J, Yin L, Qu Y, Wu J, England CG, Graves SA, Lewis CM, Wang P, Meyerand ME, Nickles RJ, Bian XW, Cai W. Targeting CD146 with a 64Cu-labeled antibody enables in vivo immunoPET imaging of high-grade gliomas. Proc Natl Acad Sci U S A. 2015; 112(47):E6525–34. [PubMed: 26553993]
20. Hernandez R, Sun H, England CG, Valdovinos HF, Ehlerding EB, Barnhart TE, Yang Y, Cai W. CD146-targeted immunoPET and NIRF Imaging of Hepatocellular Carcinoma with a Dual-Labeled Monoclonal Antibody. Theranostics. 2016; 6(11):1918–33. [PubMed: 27570560]
21. Sun H, England CG, Hernandez R, Graves SA, Majewski RL, Kamkaew A, Jiang D, Barnhart TE, Yang Y, Cai W. ImmunoPET for assessing the differential uptake of a CD146-specific monoclonal antibody in lung cancer. Eur J Nucl Med Mol Imaging. 2016; 43(12):2169–2179. [PubMed: 27342417]

22. Luo H, Hernandez R, Hong H, Graves SA, Yang Y, England CG, Theuer CP, Nickles RJ, Cai W. Noninvasive brain cancer imaging with a bispecific antibody fragment, generated via click chemistry. Proc Natl Acad Sci U S A. 2015; 112(41):12806–11. [PubMed: 26417085]
23. Westrom S, Bonsdorff TB, Abbas N, Bruland OS, Jonasdottir TJ, Maelandsmo GM, Larsen RH. Evaluation of CD146 as Target for Radioimmunotherapy against Osteosarcoma. PLoS One. 2016; 11(10):e0165382. [PubMed: 27776176]
24. Wang P, Qu Y, Li C, Yin L, Shen C, Chen W, Yang S, Bian X, Fang D. Bio-functionalized dense-silica nanoparticles for MR/NIRF imaging of CD146 in gastric cancer. Int J Nanomedicine. 2015; 10:749–63. [PubMed: 25653520]
25. Vosjan MJ, Perk LR, Visser GW, Budde M, Jurek P, Kiefer GE, van Dongen GA. Conjugation and radiolabeling of monoclonal antibodies with zirconium-89 for PET imaging using the bifunctional chelate p-isothiocyanatobenzyl-desferrioxamine. Nat Protoc. 2010; 5(4):739–43. [PubMed: 20360768]
26. Wu N, Kang CS, Sin I, Ren S, Liu D, Ruthengael VC, Lewis MR, Chong HS. Promising bifunctional chelators for copper 64-PET imaging: practical (64)Cu radiolabeling and high in vitro and in vivo complex stability. J Biol Inorg Chem. 2016; 21(2):177–84. [PubMed: 26666778]
27. Cooper MS, Ma MT, Sunassee K, Shaw KP, Williams JD, Paul RL, Donnelly PS, Blower PJ. Comparison of (64)Cu-complexing bifunctional chelators for radioimmunoconjugation: labeling efficiency, specific activity, and in vitro/in vivo stability. Bioconjug Chem. 2012; 23(5):1029–39. [PubMed: 22471317]
28. Nomine Y, Choulier L, Trave G, Vernet T, Altschuh D. Antibody Binding Selectivity: Alternative Sets of Antigen Residues Entail High-Affinity Recognition. PLoS One. 2015; 10(12):e0143374. [PubMed: 26629896]
29. Jarantow SW, Bushey BS, Pardinas JR, Boakye K, Lacy ER, Sanders R, Sepulveda MA, Moores SL, Chiu ML. Impact of Cell-surface Antigen Expression on Target Engagement and Function of an Epidermal Growth Factor Receptor x c-MET Bispecific Antibody. J Biol Chem. 2015; 290(41): 24689–704. [PubMed: 26260789]
30. Watanabe K, Terakura S, Martens AC, van Meerten T, Uchiyama S, Imai M, Sakemura R, Goto T, Hanajiri R, Imahashi N, Shimada K, Tomita A, Kiyoi H, Nishida T, Naoe T, Murata M. Target antigen density governs the efficacy of anti-CD20-CD28-CD3 zeta chimeric antigen receptor-modified effector CD8+ T cells. J Immunol. 2015; 194(3):911–20. [PubMed: 25520398]
31. Fung AS, Lee C, Yu M, Tannock IF. The effect of chemotherapeutic agents on tumor vasculature in subcutaneous and orthotopic human tumor xenografts. BMC Cancer. 2015; 15:112. [PubMed: 25884767]
32. Moncho-Amor V, Ibanez de Caceres I, Bandres E, Martinez-Poveda B, Orgaz JL, Sanchez-Perez I, Zazo S, Rovira A, Albanell J, Jimenez B, Rojo F, Belda-Iniesta C, Garcia-Foncillas J, Perona R. DUSP1/MKP1 promotes angiogenesis, invasion and metastasis in non-small-cell lung cancer. Oncogene. 2011; 30(6):668–78. [PubMed: 20890299]
33. Kellar A, Egan C, Morris D. Preclinical Murine Models for Lung Cancer: Clinical Trial Applications. Biomed Res Int. 2015; 2015:621324. [PubMed: 26064932]
34. Liu X, Liu J, Guan Y, Li H, Huang L, Tang H, He J. Establishment of an orthotopic lung cancer model in nude mice and its evaluation by spiral CT. J Thorac Dis. 2012; 4(2):141–5. [PubMed: 22833819]
35. Hiroshima Y, Zhang Y, Zhang N, Uehara F, Maawy A, Murakami T, Mii S, Yamamoto M, Miwa S, Yano S, Momiyama M, Mori R, Matsuyama R, Chishima T, Tanaka K, Ichikawa Y, Bouvet M, Endo I, Hoffman RM. Patient-derived orthotopic xenograft (PDOX) nude mouse model of soft-tissue sarcoma more closely mimics the patient behavior in contrast to the subcutaneous ectopic model. Anticancer Res. 2015; 35(2):697–701. [PubMed: 25667448]
36. Hinton PR, Xiong JM, Johlfs MG, Tang MT, Keller S, Tsurushita N. An engineered human IgG1 antibody with longer serum half-life. J Immunol. 2006; 176(1):346–56. [PubMed: 16365427]
37. Anderson CJ, Connett JM, Schwarz SW, Rocque PA, Guo LW, Philpott GW, Zinn KR, Meares CF, Welch MJ. Copper-64-labeled antibodies for PET imaging. J Nucl Med. 1992; 33(9):1685–91. [PubMed: 1517844]

38. Bleeker WK, Teeling JL, Hack CE. Accelerated autoantibody clearance by intravenous immunoglobulin therapy: studies in experimental models to determine the magnitude and time course of the effect. Blood. 2001; 98(10):3136–42. [PubMed: 11698302]

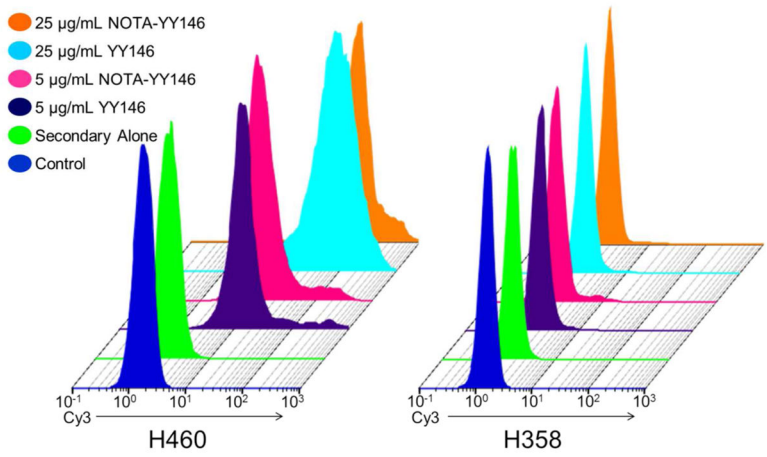

Figure 1.

The binding and immunoreactivity of YY146 and NOTA-YY146 in lung cancer cell lines was determined via flow cytometry. H460 (CD146-High) and H358 (CD146-Low) cells were incubated PBS (control; blue), 2° antibody alone (green), 5 µg/mL YY146 (purple), 5 µg/mL NOTA-YY146 (pink), 25 µg/mL YY146 (cyan), or 25 µg/mL NOTA-YY146 (orange).

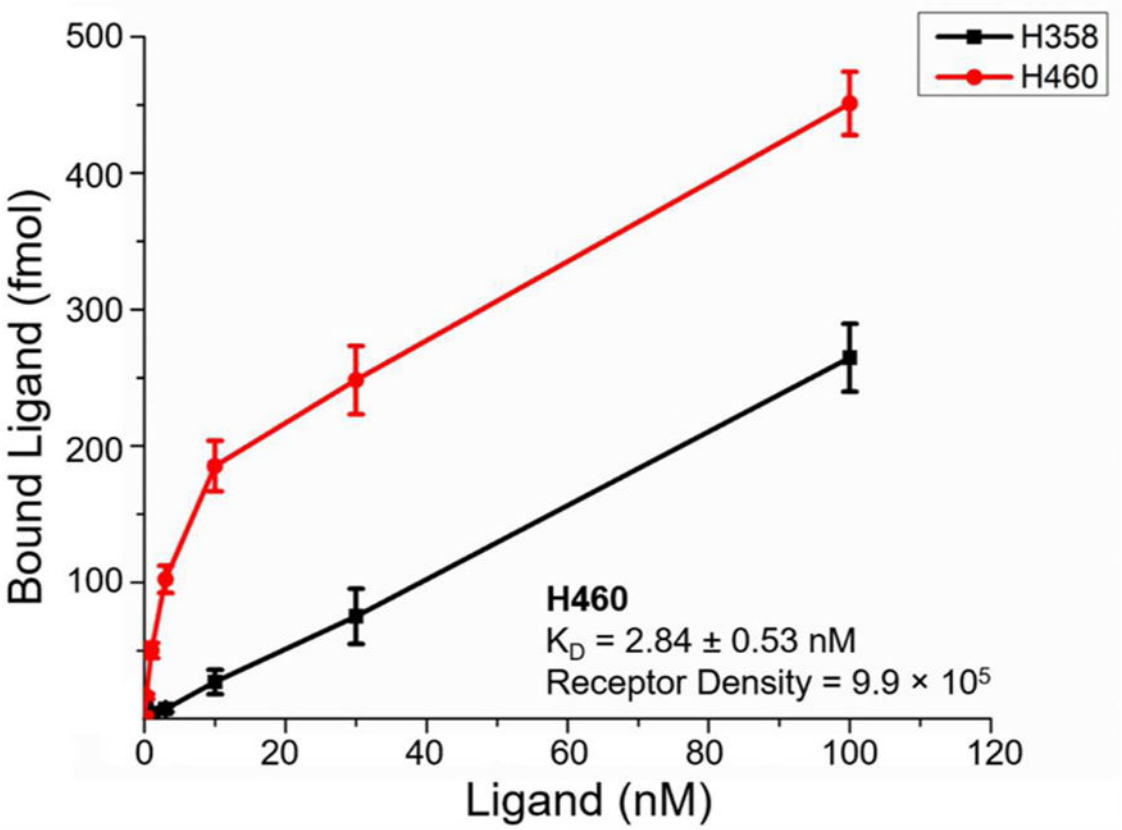

Figure 2.

CD146 saturation binding curve in lung cancer cell lines with total binding plotted as y-axis. The K_D and receptor density values were calculated as 2.84 ± 0.53 nM and 9.9 × 10^5 receptors per cell in the H460 cell line, respectively. The receptor density and K_D values corresponding to H358 cells could not be determined reliably.

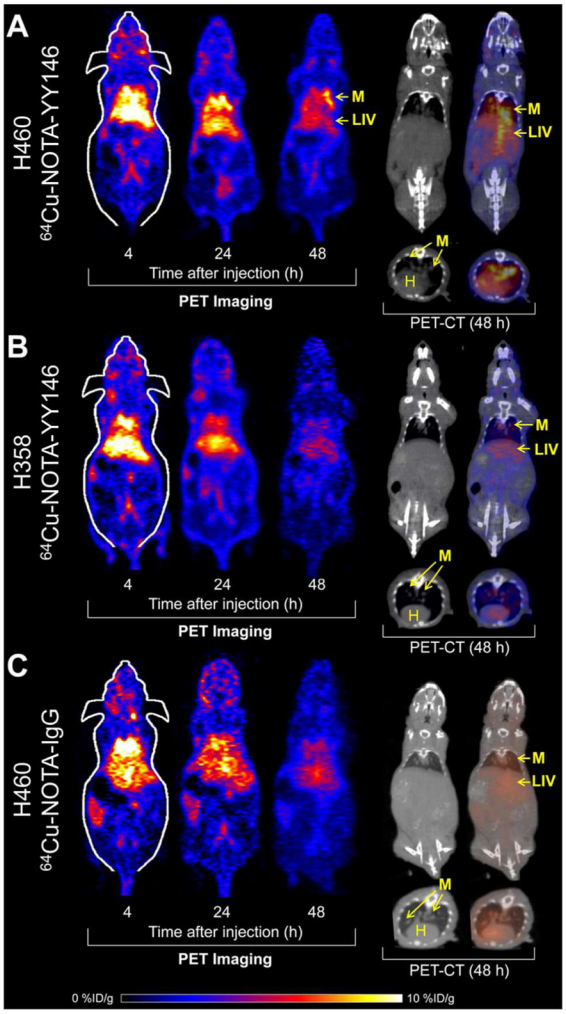

Figure 3.

PET/CT imaging of CD146 in intrapulmonary metastasissis model of NSCLC. Representative coronal PET slices showing the lungs are provided. **(A)** H460 tumor-bearing mice show increasing uptake of the tracer by 48 h post-injection. PET/CT imaging at 48 h post-injection shows signal in the intrapulmonary metastases (M), heart (H), and liver (LIV). **(B)** H358 tumor-bearing mice showed weak tumor signal that remains consistent throughout the study. PET/CT imaging at 48 h post-injection shows signal in the intrapulmonary metastases (M), heart (H), and liver (LIV). **(C)** A non-specific antibody was injected into H460 tumor-bearing mice. PET/CT imaging at 48 h post-injection shows minimal signal in the intrapulmonary metastases (M), heart (H), and liver (LIV).

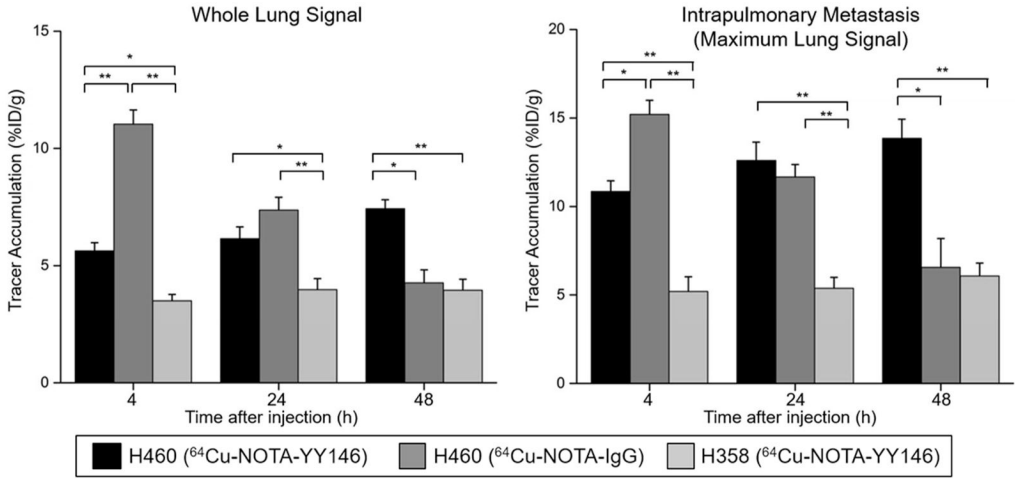

Figure 4.

Analysis of whole lung average signal and maximum lung signal derived from ROI quantification of PET images. Signal in the whole lung of H460-bearing mice increased from 4 to 24 h post-injection. The maximum lung signal corresponded to the highest signal found in a single tumor nodule. H460 tumor-bearing mice showed significantly higher maximum and average lung uptake compared to their H358 counterparts. The non-specific IgG showed high initial uptake in both whole lung and maximum lung values, yet both rapidly declined by 48 h post-injection. Results were expressed as %ID/g (mean ± SD) with n=4. * p-value ≤ 0.05, ** p-value ≤ 0.01.

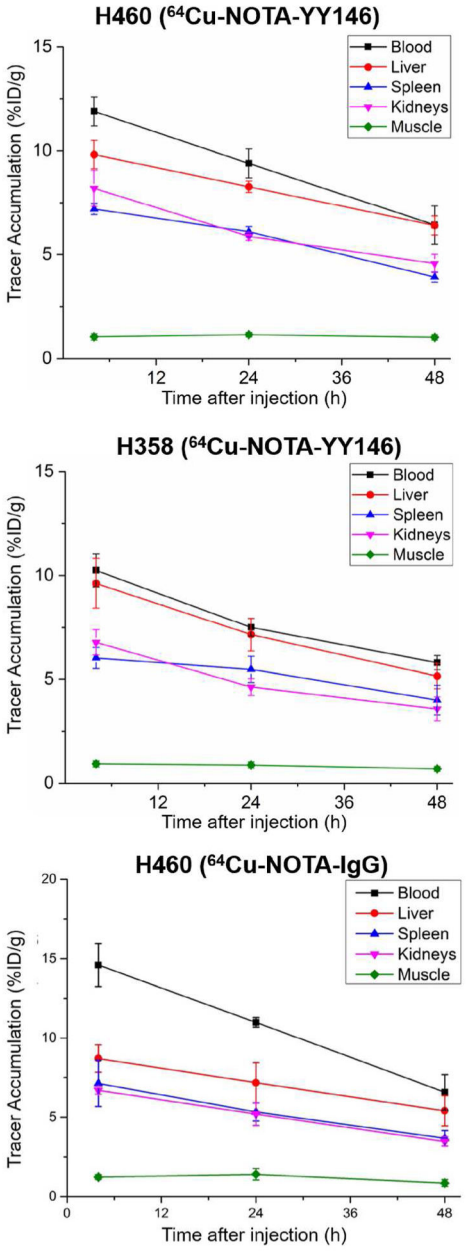

Figure 5.

PET image-derived time-activity curves showing the biodistribution of the tracers (^{64}Cu-NOTA-YY146 and ^{64}Cu-NOTA-IgG) in H460 and H358 tumor-bearing mice. The TACs revealed that the clearance behavior of the tracer from the blood pool was similar between both models. The other organs (liver, spleen, kidney, muscle) showed similar trends. Results were expressed as %ID/g (mean ± SD).

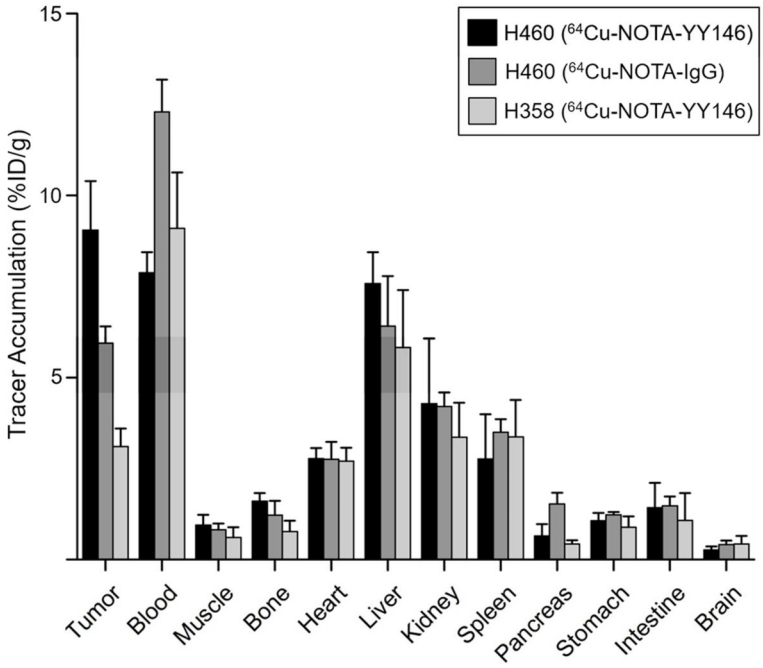

Figure 6.

Ex vivo biodistribution of the tracers (^{64}Cu-NOTA-YY146 and ^{64}Cu-NOTA-IgG) in H460 and H358 tumor-bearing mice. Mice were euthanized at 48 h post-injection and tracer biodistribution in the tumor and normal tissues was determined via gamma counting. Results were expressed as %ID/g (mean ± SD).

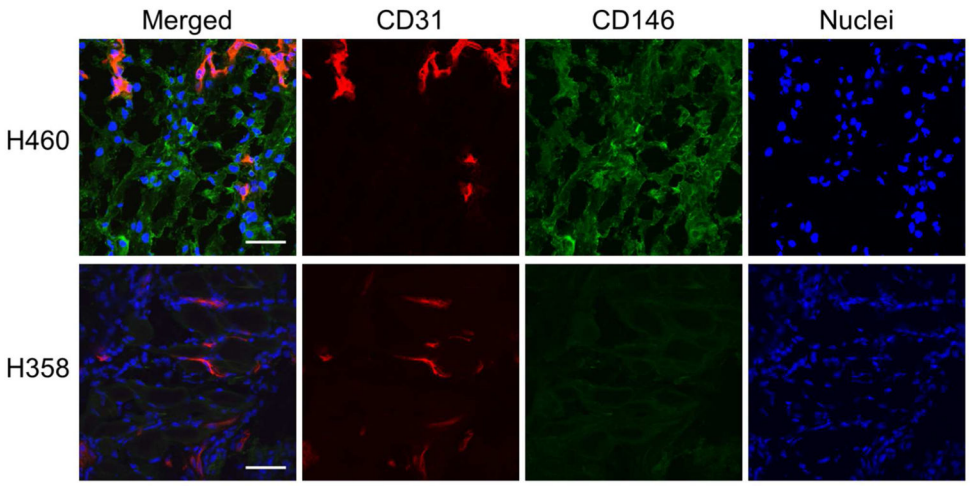

Figure 7.

CD146 and CD31 co-staining of lung tumor sections from H460 and H358 tumor-bearing mice. CD146 staining (green) was elevated in H460 sections, while only background signal was visible in H358 sections. CD31 staining (red) revealed similar degrees of vasculature between both tumor models. Scale bar = 100 μm.